



ARTICLE

Open Access

Observation of nonlinear disclination states

Boquan Ren¹, Antonina A. Arkhipova^{2,3}, Yiqi Zhang¹ , Yaroslav V. Kartashov² , Hongguang Wang¹, Sergei A. Zhuravitskii^{2,4}, Nikolay N. Skryabin^{2,4}, Ivan V. Dyakonov⁴, Alexander A. Kalinkin^{2,4}, Sergei P. Kulik⁴, Victor O. Kompanets², Sergey V. Chekalin² and Victor N. Zadkov^{2,3}

Abstract

Introduction of controllable deformations into periodic materials that lead to disclinations in their structure opens novel routes for construction of higher-order topological insulators hosting topological states at disclinations. Appearance of these topological states is consistent with the bulk-disclination correspondence principle, and is due to the filling anomaly that results in fractional charges to the boundary unit cells. So far, topological disclination states were observed only in the linear regime, while the interplay between nonlinearity and topology in the systems with disclinations has been never studied experimentally. We report here on the experimental observation of the nonlinear photonic disclination states in waveguide arrays with pentagonal or heptagonal disclination cores inscribed in transparent optical medium using the fs-laser writing technique. The transition between nontopological and topological phases in such structures is controlled by the Kekulé distortion coefficient r with topological phase hosting simultaneously disclination states at the inner disclination core and spatially separated from them corner-I, corner-II, and extended edge states at the outer edge of the structure. We show that the robust nonlinear disclination states bifurcate from their linear counterparts and that location of their propagation constants in the gap and, hence, their spatial localization can be controlled by their power. Nonlinear disclination states can be efficiently excited by Gaussian input beams, but only if they are focused into the waveguides belonging to the disclination core, where such topological states reside. Our results open new prospects for investigation of nonlinear effects in topological systems with disclinations and are relevant for different areas of science, including Bose-Einstein and polariton condensates, where potentials with the disclinations can be created.

Introduction

Topological systems hosting topologically protected states at their edges or in their corners are attracting considerable attention in diverse areas of physics, including solid-state physics^{1,2}, mechanics³, acoustics⁴, physics of matter waves⁵, exciton-polariton condensates⁶, and, particularly, in photonics^{7–9}. This attention is connected, in part, with considerable practical potential of topological systems for

construction of transmission lines, switching devices, routers, and lasers resilient to disorder and edge deformations. With the development of topological photonics^{7–9}, the class of systems, where topologically nontrivial states can be encountered has been substantially extended. While many works on photonic topological insulators employed periodic in the bulk structures for demonstration of topologically protected edge states^{10–17}, it is now realized that the topological insulators can also be created using aperiodic structures that possess discrete rotational symmetry, but lack periodicity, such as quasi-crystals¹⁸, fractal structures^{19,20}, and structures with disclinations^{21–23}.

The concept of topological insulators with disclinations originates from solid state physics^{24–28}, where it was predicted that disclinations — crystallographic defects disrupting lattice structure — can trap fractional “spectral” charges

Correspondence: Yiqi Zhang (zhangyiqi@xjtu.edu.cn) or Yaroslav V. Kartashov (yartashov@icfo.eu)

¹Key Laboratory for Physical Electronics and Devices, Ministry of Education, School of Electronic Science and Engineering, Xi'an Jiaotong University, Xi'an 710049, China

²Institute of Spectroscopy, Russian Academy of Sciences, Troitsk, Moscow 108840, Russia

Full list of author information is available at the end of the article

These authors contributed equally: Boquan Ren, Antonina A. Arkhipova

© The Author(s) 2023



Open Access This article is licensed under a Creative Commons Attribution 4.0 International License, which permits use, sharing, adaptation, distribution and reproduction in any medium or format, as long as you give appropriate credit to the original author(s) and the source, provide a link to the Creative Commons license, and indicate if changes were made. The images or other third party material in this article are included in the article's Creative Commons license, unless indicated otherwise in a credit line to the material. If material is not included in the article's Creative Commons license and your intended use is not permitted by statutory regulation or exceeds the permitted use, you will need to obtain permission directly from the copyright holder. To view a copy of this license, visit <http://creativecommons.org/licenses/by/4.0/>.

(connected with the local density of states^{21,29}) and support localized states of the topological origin. Such systems can also be used³⁰ for realization of the higher-order topological insulators hosting so-called zero-dimensional states³¹. The bulk-disclination correspondence principle proposed for these systems that links the appearance of the disclination states with the topological properties of the spectrum, illustrates the importance of fractional spectral charges as a probe of “crystalline” topology of these systems^{21,22,32}. Higher-order topological disclination states typically form at the boundary of the hollow disclination core of the structure. It has been demonstrated that linear lattices with disclinations offer new opportunities for the control of confinement and internal structure of the field, not only in photonics^{33,34}, but also in acoustics^{35–37}. Different from aforementioned achievements reported only in linear media, the impact of nonlinearity on photonic disclination states was addressed theoretically only recently³⁸, while experimental observation of nonlinear disclination states has never been performed so far.

At the same time, nonlinear effects, such as self-action of light, attract more and more attention in topological photonics⁹ because they enable all-optical control of the properties of the topological states. New effects of topological origin emerging due to self-action include topological phase transitions³⁹, nonlinear Thouless pumping^{40–43}, formation of the topological solitons^{44–53}, development of the modulational instabilities of the edge states^{54,55} and rich bistability effects^{56,57}, to name only a few. Nonlinear higher-order topological insulators supporting corner solitons have been also reported theoretically⁵⁸ and in experiment^{59,60}, while the Floquet version of higher-order nonlinear topological insulator was proposed just recently⁶¹.

Disclination states appearing in aperiodic structures obtained by specific deformations of periodic arrays, formally belong to a class of higher-order topological states. However, in contrast to the previously considered higher-order insulator geometries with periodic bulk, disclination systems may feature other types of discrete rotational symmetries, not compatible with crystallographic symmetries and not attainable in usual higher-order insulators. One can thus expect that such symmetry properties of the disclination systems should find their manifestation in a completely different structure of their linear eigenmodes, properties of nonlinear self-sustained states bifurcating from them, and in their excitation dynamics. Our work is thus aimed at the exploration of the interplay of nonlinear self-action effects and topology in the disclination structures with different discrete rotational symmetries.

Here we report on the first experimental observation of the nonlinear topological states in disclination arrays with both pentagonal and heptagonal cores, obtained by removing or adding sectors into periodic honeycomb structures, where topological phase arises due to the Kekulé distortion^{12,16,21,23,29} introduced into positions of six sites in

each unit cell of the structure. Our disclination arrays are inscribed in nonlinear fused silica, using the fs-laser direct writing technique^{10,59,62–65}. In contrast to the previously observed disclination states in linear photonic crystals constructed from the arrays of dielectric cylinders²¹, here we study how the nonlinear response of fused silica, which becomes pronounced for the pulsed excitations from high-power laser, can strongly affect the properties and localization of the disclination states in laser-written structures, thereby stressing that the nonlinearity offers a convenient knob for control of excitations in the topological systems. Moreover, we study here the disclination arrays with different discrete rotational symmetries, illustrating that the topological solitons in them are universal and can emerge in a wide variety of such structures. We observe that when disclination arrays are in topological phase, one can excite thresholdless disclination solitons existing in a broad range of input powers by Gaussian beam focused into one of the waveguides on the disclination core. The excitation of the same waveguides in nontopological regime yields strong diffraction at low powers, while formation of nontopological self-sustained states occurs only above considerable power threshold. We thus compare behaviour of nonlinear excitations for different values of the distortion coefficient r . The results obtained here are relevant for a broad class of nonlinear physical systems, including matter waves, polariton condensates, photonic crystals, atomic vapors, and many others, where potentials with disclinations can be created. They also highlight the potential of these topological structures for realisation of higher-harmonic generation and lasing that may benefit from strong topological state confinement and its resilience to disorder.

Results

Spectra of the arrays with disclinations

We consider paraxial propagation of a light beam along the z axis of a medium with the focusing cubic nonlinearity and shallow transverse refractive index modulation that can be described by the nonlinear Schrödinger-like equation for the dimensionless light field amplitude ψ :

$$i \frac{\partial \psi}{\partial z} = -\frac{1}{2} \left(\frac{\partial^2}{\partial x^2} + \frac{\partial^2}{\partial y^2} \right) \psi - \mathcal{R}(x, y) \psi - |\psi|^2 \psi \quad (1)$$

where x, y are the scaled transverse coordinates, z is the propagation distance that plays the same role as time in the Schrödinger equation describing a quantum particle in a potential, and the function $\mathcal{R}(x, y)$ describes disclination array with the straight waveguides:

$$\mathcal{R} = p \sum_{m,n} e^{-(x-x_{m,n})^2/a_x^2 - (y-y_{m,n})^2/a_y^2}$$

where a_x and a_y are the widths of waveguides that are elliptical due to the writing process, $x_{m,n}$ and $y_{m,n}$ are the

positions of the waveguide centers (depending on the particular type of introduced disclination), and p is the array depth proportional to the refractive index contrast δn in the structure (see “Methods” for adopted normalizations). To create topologically nontrivial arrays with disclinations we use two-step process. We start from usual periodic honeycomb waveguide array with identical waveguide spacing d in the entire structure and first introduce shift of the waveguides in the direction perpendicular to the borders of the unit cell, whose magnitude can be characterized by the Kekulé distortion coefficient $r = \ell_{\text{intra}}/\ell_{\text{inter}}$, with ℓ_{intra} and ℓ_{inter} being intra-cell and inter-cell spacing between waveguides after shift^{12,16,21,23}. Clearly, $r=1$ corresponds to non-deformed structure with $\ell_{\text{intra}} = \ell_{\text{inter}} = d$. As it will be shown below, by changing the value of r one can achieve the transition between topologically trivial and nontrivial geometries. On the second step, to create the arrays with disclination, we remove or add sectors into honeycomb structure with shifted waveguides. At this step, after removing of the sector we deform the unit cells in the remaining structure such that they fill the entire 2π polar angle, while to add the sector we compress unit cells accordingly (see “Methods” for the description of the deformation process).

In Fig. 1a, we display the microphotographs of the arrays with pentagonal disclination core inscribed with fs-laser in 10 cm long fused silica sample (total number of waveguides in this structure is 90), obtained by removing a sector from honeycomb array, with coordinates of the waveguides obtained using the above two-step process for three different values of the distortion coefficient r . Black hexagons filled with different background colors are superimposed on the microphotographs as guides for the eye indicating different cells of the structure. The color of the background is selected in accordance with position of the cells, as indicated in the figure caption. Similar microphotographs, but for the structure with the heptagonal disclination core (total number of waveguides is 126) that was obtained by adding the sector into honeycomb array are presented in Fig. 1d, also for three different r values. While the main focus of this work is the interplay between the nonlinearity and topology in the systems with disclinations, we consider experimentally the systems with different symmetries. For instance, we also consider heptagonal structures, where disclination states were not reported experimentally so far, as mainly pentagonal structures were employed in previous linear experiments²¹.

Topological properties of these structures are controlled by the distortion coefficient r . One can see that for $r < 1$ the inter-cell coupling becomes weaker than the intra-cell one, while for $r > 1$ the situation is reversed, and the inter-cell coupling becomes stronger than the intra-cell one,

indicating on the possible transition of the disclination array into higher-order topological insulator phase. This transition is manifested in qualitative modification of the linear spectrum of eigenmodes supported by these structures. To obtain such modes, we first use the ansatz $\psi = u(x, y)e^{ibz}$, where b is the propagation constant and $u(x, y)$ is the real function, for Eq. (1) to get the equation

$$bu = \frac{1}{2} \left(\frac{\partial^2}{\partial x^2} + \frac{\partial^2}{\partial y^2} \right) u + \mathcal{R}u + u^3 \quad (2)$$

We then omit last nonlinear term in Eq. (2) and calculate all linear eigenmodes of the system numerically (see “Methods” for description of the employed plane-wave expansion method). The present system can also be analyzed using the tight-binding model that is well-suited for the description of light propagation in fs-laser written waveguides⁶⁶. At the same time, we would like to stress that the continuous model adopted here enables more accurate description of light propagation in array because it accounts for real refractive index landscape in the sample, i.e. ellipticity of the waveguides and coupling between all sites of the structure, it takes into account radiation from the waveguides and variation of the field inside the waveguides that is not considered in discrete systems.

The transformation of linear spectrum of the array with the pentagonal disclination core with increase of the distortion coefficient r is illustrated in Fig. 1b. While at $r < 1$ no localized states are present in the gap between two bulk bands, at $r > 1$ the spectrum changes qualitatively, with several different types of localized states emerging in the gap. The appearance of such states can be explained by the bulk-disclination correspondence principle, which gives the link between the fractional charge and topologically nontrivial states (see “Methods” for discussion of the topological invariants). Among these states, five states marked with orange color (their number is dictated by the symmetry of the structure) are disclination states residing at the disclination core in the center of the array. Some of these states can be degenerate depending on the value of r , but in general they have different eigenvalues. These states have different phase structure, their localization at the disclination core increases with the increase of r . To describe the structure of the spectrum in more details, we chose $r = 1.68$ [cyan dashed line in Fig. 1b] and show eigenvalues of all modes in the interval $0.36 \leq b \leq 0.50$ in Fig. 1c. Besides disclination states, in the same gap there appear corner-I (dark-green dots), edge (purple dots), and corner-II states (green dots), but all of them emerge at the outer edge/corners of the structure due to its finite size and on this reason they do not hybridize for sufficiently large r with orange disclination states localized on the central disclination core. Calculated intensity distributions of all eigenmodes forming in the gap at $r = 1.68$ for the arrays with pentagonal and

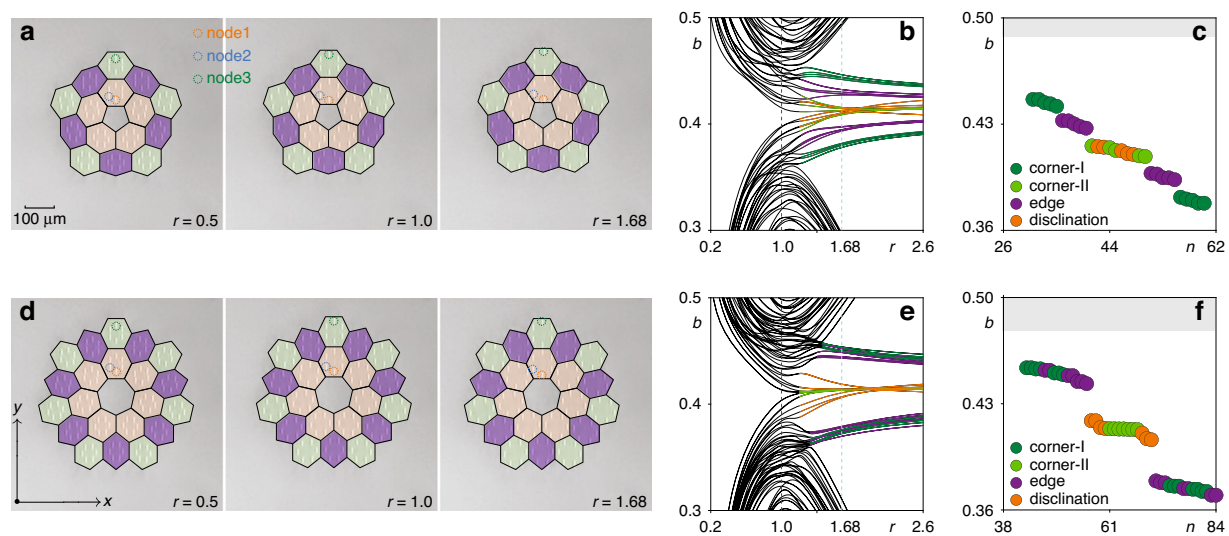


Fig. 1 Disclination arrays and their linear spectra. **a** Microphotographs of the fs-laser written waveguide arrays with a pentagonal disclination core for different values of the distortion coefficient r . The orange, blue, and green dotted circles indicate the nodes 1, 2 and 3, that will be used below for probing of excitation dynamics. Unit cells near the disclination core, at the edges or in the corners of the array are marked with orange, purple and green colors, respectively. **b** Propagation constants b of the eigenmodes of pentagonal disclination array vs distortion coefficient r . Orange curves are associated with states residing at the disclination core. **c** Spectrum at $r = 1.68$. The bands corresponding to the bulk states are shown in gray, while propagation constants of corner-I, corner-II, edge and disclination states are represented by dots of different colors. **d–f** Microphotographs and spectrum for the array with heptagonal disclination core. The arrangement of panels is the same as in (a–c)

heptagonal disclination cores are presented in Supplementary Materials — to stress generality of these results, we present them for even larger structures with 300 (420) waveguides for pentagonal (heptagonal) cases — while in experiments we use sufficiently large and most compatible with writing technology structures from Fig. 1.

Similar transformation of linear spectrum with increase of r is observed also in the array with heptagonal disclination core, see Fig. 1d. In this structure seven disclination states with different phase structures emerge in the spectrum (some of them are nearly degenerate so that there are seemingly five orange curves) shown in Fig. 1e. Detailed structure of spectrum for this case is presented in Fig. 1f for $r = 1.68$, where one can again see that disclination states at the disclination core may coexist with spatially separated from them corner-I (dark-green dots), edge (purple dots), and corner-II states (green dots) at the outer edge. The symmetry of the heptagonal array is different from that of the pentagonal array, therefore their corresponding gap widths are different, and this is also the reason why the corner states cross/overlap with edge states in Fig. 1e when $r > 1$, but not in Fig. 1b.

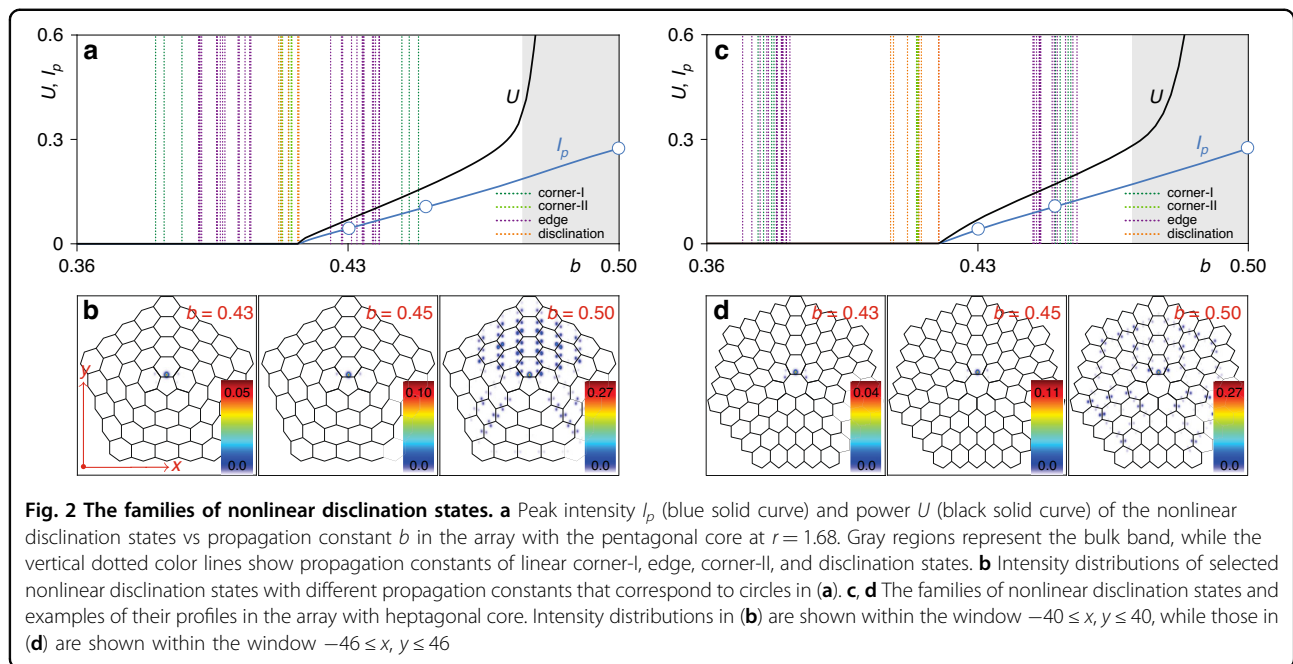
We would like to note that the corner-II states present in the spectrum have different internal structure from the corner-I state which has intensity maximum in the very corner site. In contrast, in corner-II state there is no light in this site. In tight-binding models, the corner-II states usually emerge at zero “eigenvalues”¹⁶, so they are

frequently named also “zero-energy states”. Here, for convenience, we distinguish them by using notations “corner-I” and “corner-II” states. Due to different parity of corner-I and corner-II states only the former one is efficiently excited by injecting a Gaussian beam into the corner site, while the latter requires more sophisticated excitation configurations, for example with two out-of-phase beams. It is also worth noting that corner-II and disclination states do not hybridize in topological regime even though their propagation constants may cross at certain r (they do not overlap for all r values). Hybridization is unavoidable only at $r \rightarrow 1$ because in this limit the states substantially broaden, so that the coupling between them may occur in finite-size structure.

The emergence of disclination states of topological origin at the inner disclination core is consistent with the bulk-disclination correspondence principle^{21,22,32} that establishes the link between the fractional disclination charge Q (see “Methods” for details of topological characterization) and the localized states emerging at the disclination core. For our arrays, $Q = 1/2$ in topologically nontrivial phase at $r > 1$ signaling on the appearance of disclination states, while $Q = 0$ in nontopological regime, when $r < 1$ and disclination states are absent.

Properties of nonlinear disclination states

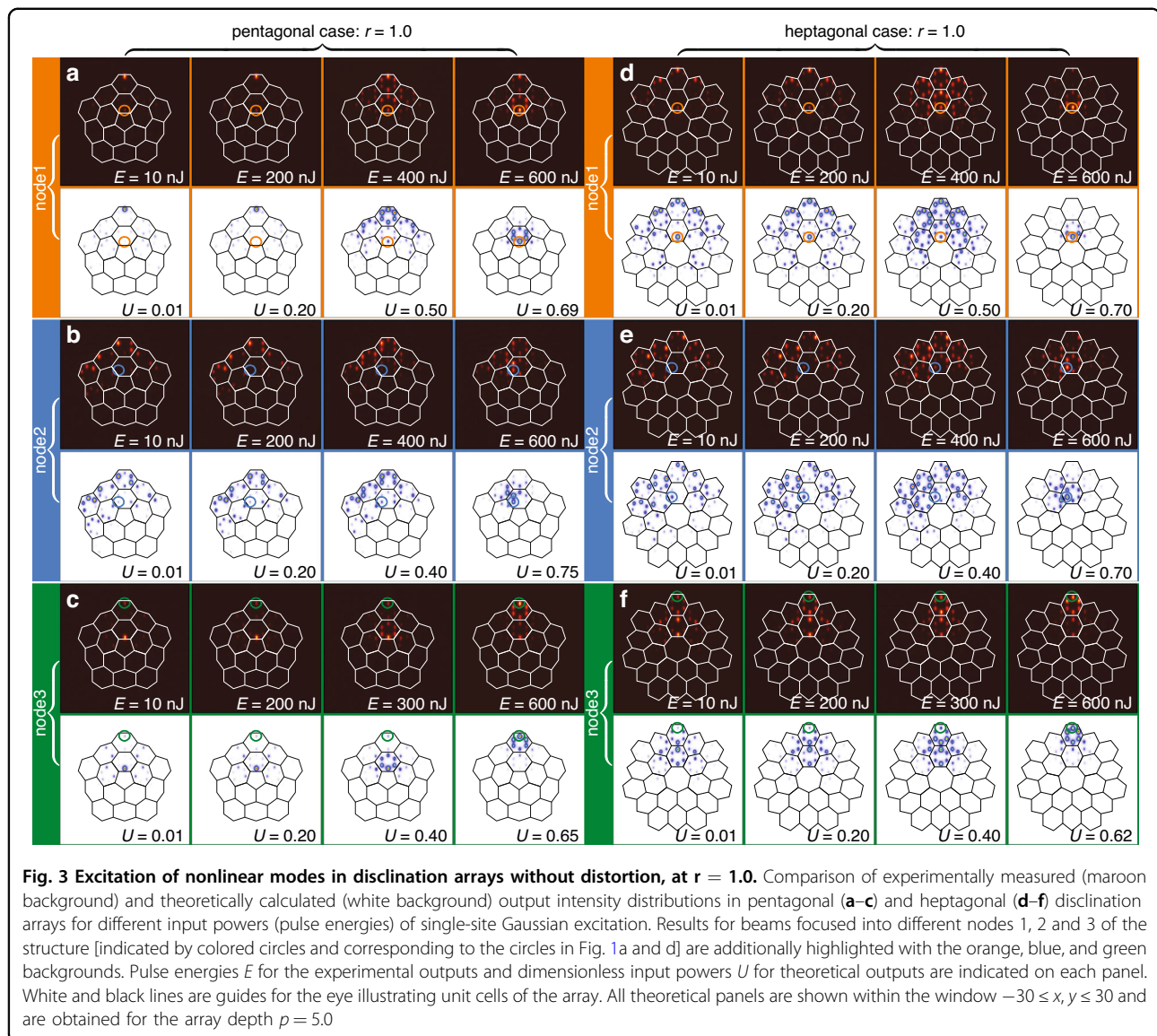
We now address the properties of stationary nonlinear disclination states, whose shapes are governed by the



Eq. (2), where we keep the last nonlinear term. Such states can be found using the Newton relaxation method (see “Methods” for details). By analogy with corner solitons encountered in higher-order topological insulators with periodic bulk^{59,60}, such nonlinear disclination states can be called disclination solitons. For their theoretical description we adopt the large-scale disclination arrays schematically depicted in Fig. 2. In both pentagonal and heptagonal arrays the families of the nonlinear disclination states bifurcate from linear modes localized at the disclination core. We consider bifurcation from the disclination state with the largest propagation constant (see Supplementary Materials). With the increase of the propagation constant b the power $U = \iint |\psi|^2 dx dy$ of nonlinear disclination state monotonically grows [see Fig. 2a and c for pentagonal and heptagonal cases, respectively], while the state first rapidly localizes and already at $U \sim 0.1$ concentrates practically on one side of the disclination core [see representative intensity distributions in Fig. 2b and d]. This clearly stresses solitonic nature of such state, since without nonlinearity its power would be redistributed between different sites at the disclination core due to beating between several disclination states (notice that this process may be slow because eigenvalues of linear disclination states are close). The peak intensity $I_p = \max\{|\psi|^2\}$ of nonlinear disclination state [blue curve in Fig. 2a and c] practically linearly increases with b . Even though propagation constant of the nonlinear disclination state crosses eigenvalues of linear edge (purple vertical dashed lines) and corner-I (dark green vertical dashed lines) states, no coupling with them occurs because they are located at the outer edge of the array. However, when

the propagation constant of the nonlinear disclination state penetrates into the bulk band, shown with gray color in Fig. 2a and c, the coupling with bulk states occurs that leads to strong expansion over entire array [see right panels in Fig. 2b and d]. As a result, the power U in the band rapidly increases with increase of b . These results illustrate that nonlinear disclination states are the modes of topological origin, whose position inside the gap and localization degree strongly depend on their power. This reveals one of the main advantages that nonlinearity offers in this system: one can tune the location of the disclination state propagation constant in the forbidden gap by changing its power. Stability of the nonlinear disclination states was analyzed by adding a small-scale perturbation (5% in amplitude) to them and propagating them in the frames of Eq. (1) over a very long distance $z \sim 4000$ that by several orders of magnitude exceeds available sample length. The propagation was modelled using the split-step fast Fourier transform method. This analysis shows that all such states in the gap are stable in both pentagonal and heptagonal arrays. Notice that we use different backgrounds to distinguish unit cells in different regions only on images showing arrays (see Figs. 1 and 6), while intensity distributions, like those shown in Fig. 2, will have the same background.

In Eq. (1), the nonlinearity is focusing, which corresponds to our experiments performed with arrays written in fused silica samples. At the same time, solitons on disclinations are universal and can also be obtained in defocusing materials. Thus, in Supplementary Materials, we present an example of such soliton family obtained in the frames of Eq. (1) with the opposite sign of the



nonlinear term. Moreover, such states can also be potentially obtained in materials with saturable nonlinearities, typical for example for photorefractive crystals^{52,60,67}. The examples of such states in saturable media are also included in Supplementary Materials.

Observation of nonlinear disclination states

For observation of nonlinear disclination states we inscribed (see “Methods” for details of fabrication) the arrays with pentagonal and heptagonal disclination cores with different values of the distortion coefficient $r = 0.8$, 1.0 and 1.68, to be able to compare dynamics in topologically trivial and nontrivial structures. In experiments, we employed single-waveguide excitations using femtosecond pulses of variable energy E from 1 kHz Ti:sapphire laser at 800 nm central wavelength. Initially, short pulses

with a 40 fs duration and wide spectrum from a regenerative amplifier system Spitfire HP (Spectra Physics) first pass through an active beam position stabilization system (Avesta) and an attenuator, and afterwards are launched into a 4f single-grating stretcher-compressor with a variable slit. Spectra of such pulses are narrowed by a slit down to 5 nm, which corresponds to the pulse duration of 280 fs. This increase in pulse duration allows to prevent optical collapse and strong spectral broadening during pulse propagation in the waveguides, i.e. it allows to neglect the temporal effects. The pulses after stretcher-compressor were focused into selected waveguides and the output intensity distributions after propagation in the sample were recorded using a Kiralux CMOS camera (Thorlabs). The input peak power in the waveguide (for each pulse in the 1 kHz sequence) was defined as a ratio of

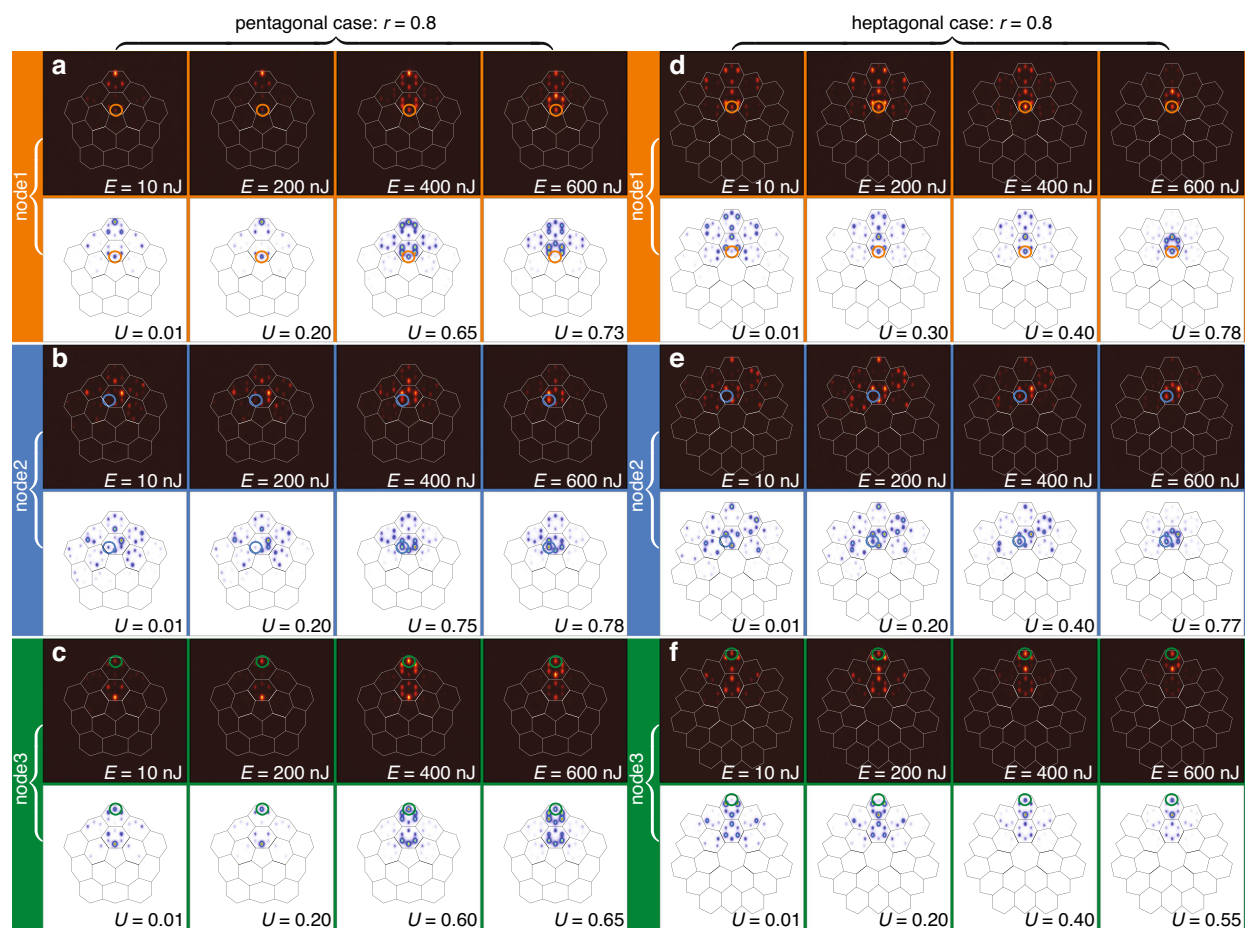
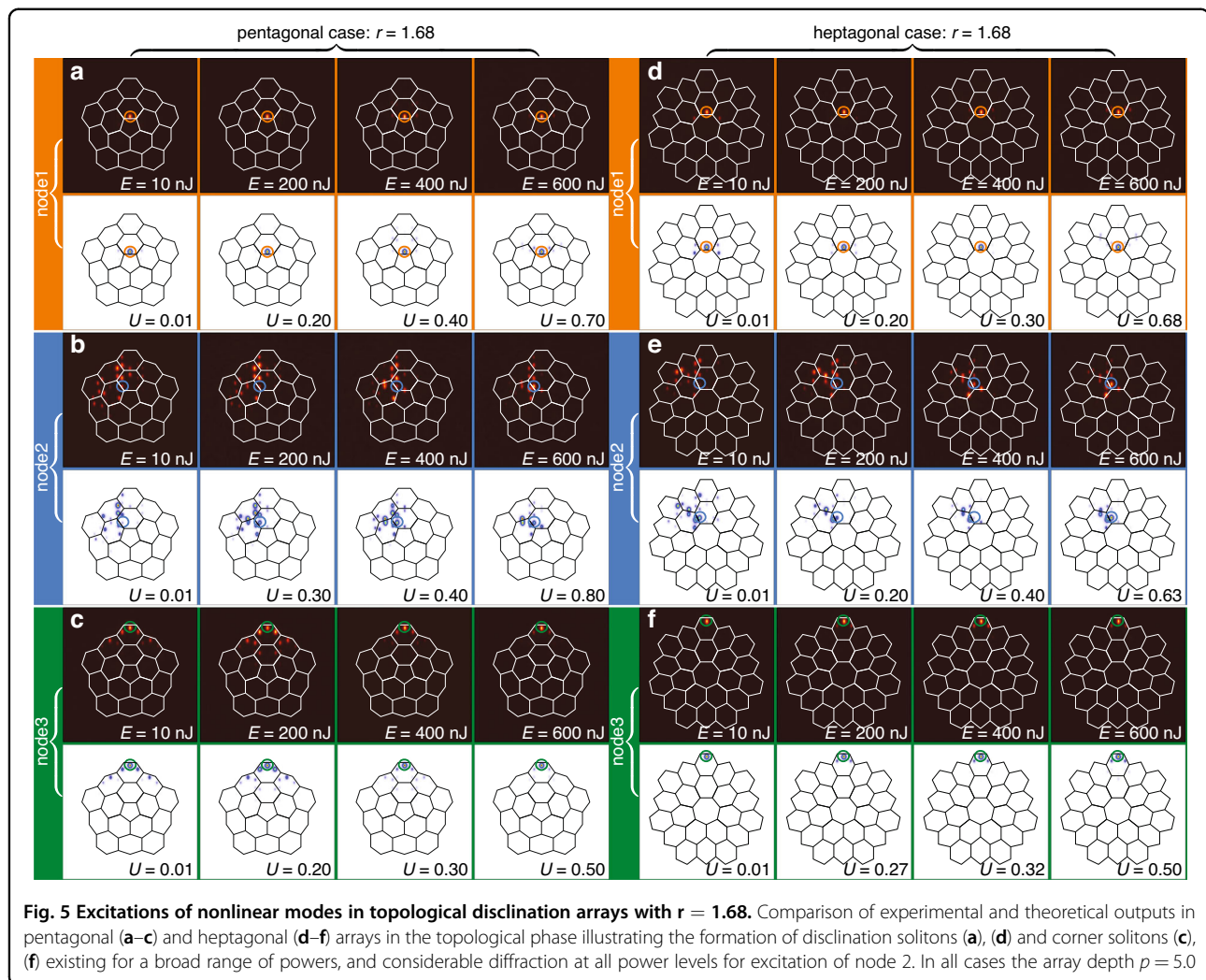


Fig. 4 Excitation of nonlinear modes in nontopological disclination array with $r = 0.8$. Comparison of the output theoretical and experimental output intensity distributions for different input powers in pentagonal (a–c) and heptagonal (d–f) arrays in topologically trivial phase. The arrangement of panels is similar to Fig. 3. The array depth is $p = 4.9$ in (a–c) and $p = 5.0$ in (d–f)

the input pulse energy E to the pulse duration $\tau = 280$ fs and taking into account the losses for matching with the focusing lens the input power can be evaluated as 2.5 kW for each 1 nJ. For example, maximal excitation energy of $E = 600$ nJ in experimental patterns shown in Figs. 3, 4, 5 corresponds to the peak power of 1.5 MW. We compare excitations of three different waveguides (nodes) numbered 1 (at the disclination core), 2 (in the bulk), and 3 (in the outer corner) indicated by colored circles in Fig. 1a and d. The purpose of the excitation of node 2 in the experiment is twofold. First, we would like to show that there are no localized linear states in the bulk of disclination lattice (node 2 formally belongs to the bulk of the structure) and that the localization in the bulk occurs only above certain power threshold. In clear contrast, corner-I and disclination states are thresholdless and can be easily excited in the topological regime even by low-power beams launched in nodes 3 and 1, respectively. Second, we would like to stress that to excite the disclination state, one has to launch a Gaussian beam directly

into the site belonging to the disclination core. One cannot excite it efficiently by focusing light into neighboring site to the disclination core.

In Fig. 3 we present comparison of the output intensity distributions for these three types of excitations calculated theoretically (images with white background) using Eq. (1) and measured experimentally (images with maroon background) for both pentagonal and heptagonal disclination arrays without distortion, i.e. with $r = 1$. In this “borderline” case between topological and nontopological phases, no localized states are present in spectra of the arrays. On this reason the excitation of any of the nodes 1, 2, or 3 is accompanied by strong diffraction in the linear regime for $E = 10$ nJ pulses (in Fig. 3 the position of excitation in each case is marked by colored ring), which is well visible also at intermediate propagation distances inside the sample. Increasing pulse energy (power in theoretical simulations) results in gradual contraction of light towards the excited waveguide. For excitation of node 1 at disclination core one can observe the formation



of well-localized soliton at highest shown pulse energy $E \sim 600$ nJ, i.e. above considerable threshold [Fig. 3a and d]. The same pulse energy level in general is not sufficient for soliton formation for excitation in the bulk [Fig. 3b and e] and at the outer corner [Fig. 3c and f], since at this energy level the tendency for light contraction to the excited waveguide only begins. To achieve good localization in these cases one has to increase the pulse energy even further, approximately to $E \sim 900$ nJ level. In this regime, the localization occurs because the beam creates self-induced defect in the lattice due to nonlinearity when its power exceeds certain threshold, and the resulted nontopological solitons can appear only in semi-infinite gap (above all allowed bands).

In Fig. 4 we consider the same three types of excitations in the trivial insulator phase, when distortion coefficient $r = 0.8$. According to the Wannier center analysis in each unit cell, the filling anomaly does not occur in this case, and, consequently, no localized corner-I, edge or disclination states can appear in the linear spectrum of the

system, despite the fact that forbidden gap opens for this value of r [see Fig. 1b and e], i.e. all linear eigenmodes are delocalized bulk modes. Thus, one again observes diffraction in the linear regime for $E = 10$ nJ pulses, for both pentagonal Figs. 4a–c and heptagonal Figs. 4d–f disclination arrays for all three types of excitations. Moreover, now localization does not occur for excitation at the disclination core even for pulse energies $E \sim 600$ nJ that was sufficient for nonlinear localization at $r = 1.0$. Thus, there exists the tendency for increase of the pulse energy required for localization at the disclination core with decrease of r . For depicted pulse energies localization was not observed neither for bulk nor for corner excitations (it occurs only around $E \sim 900$ nJ).

The picture changes qualitatively at $r = 1.68$ in topologically nontrivial phase. In this case, the disclination core supports topologically nontrivial localized disclination states, thus the input beam focused into node 1 excites localized states even at the lowest pulse energies $E \sim 10$ nJ in both pentagonal [Fig. 5a] and heptagonal [Fig. 5d]

arrays. Notice that even though in this quasi-linear regime single-site excitation leads to simultaneous population of several localized disclination eigenmodes, the beating between them occurs on the scale much larger than sample length (due to small difference of propagation constants b of such eigenmodes, see Supplementary Materials) and is therefore not visible in experiment at 10 cm of propagation. Even weak nonlinearity suppresses this beating leading to the formation of well-localized disclination solitons that exist over broad range of input pulse energies (powers), as long as propagation constants of such states remain in the forbidden gap of the spectrum [Fig. 5a and d]. Notice that because for $r = 1.68$ the gap is already wide, in experiment we do not reach power levels (below optical damage threshold), at which strong coupling with bulk states occurs. In contrast, when node 2 in the bulk is excited, one observes diffraction, and nonlinear localization does not occur even for pulse energies $E \sim 600$ nJ [see Fig. 5b and e]. Visual slowdown of diffraction for excitation of node 2 at $r = 1.68$ can be explained by the emergence of many close pairs of waveguides in the array, so that diffraction involves rapid light switching between such pairs, accompanied by slower gradual power transfer between neighbouring pairs. An interesting situation is encountered for excitation of the node 3 [Fig. 5c and f]. This excitation has the largest overlap with the corner-I states that are also well-localized for this value of r at the outer edge of the array, and it does not excite corner-II states (because the latter have different symmetry, see Supplementary Materials). As a result, in this case one observes the formation of nonlinear corner-I states in both pentagonal and heptagonal disclination arrays, whose localization degree only weakly changes in the considered range of input powers. Theoretical simulations fully support these observations.

Discussion

In conclusion, we have reported on the experimental observation of nonlinear disclination states in disclination lattices inscribed in transparent nonlinear optical medium. Such states form when Kekulé distortion of waveguide positions drives the array into the topological phase, where several different types of localized states appear: disclination states residing at the disclination core and not overlapping with them spatially corner-I, corner-II and edge states at the outer edge of the structure. The nonlinearity enables strong light localization on one side of the disclination core. Our findings are reported for the pentagonal and heptagonal structures, with symmetry different from previously considered higher-order insulators with periodic bulk (such as C_3 , C_4 , C_6 ones). They pave the way for the development of new types of topological lasers on disclination states, efficient harmonic generation in topologically protected states, and

observation of new interesting topological objects, such as topological Floquet disclination bound states in the continuum⁶⁸.

We would like to state that the disclination states are rather compact, and they are characterized by small mode area that is beneficial for the enhancement of nonlinear effects and for realization of stable lasing. In addition, disclination lattices with different discrete rotational symmetries may be potentially used for realisation of lasing in states with different vorticity, limited by the discrete rotational symmetry of the structure. Finally, because in these systems disclination states coexist with topological corner-II states (having distinct propagation constants), one can potentially observe switching between lasing in these two different topological modes.

Materials and methods

Fs-laser inscription of the waveguide arrays

The waveguide arrays shown in Fig. 1a, d were inscribed in 10 cm-long fused silica glass samples (JGS1) using focused (with an aspheric lens with NA = 0.3) fs-laser pulses at the wavelength of 515 nm with the duration 280 fs, repetition rate 1 MHz, and energy 320 nJ under the surface of sample at the depth range of 550–1050 μm near the preselected optimal depth of 800 μm . Translation of the sample during the writing process of each waveguide was performed by the high-precision air-bearing positioner (Aerotech) with identical for all waveguides velocity of 1 mm/s. All such waveguides are single-mode, have almost identical elliptical shapes and exhibit the propagation losses not exceeding 0.3 dB/cm at $\lambda = 800$ nm. The structures are written in the depth range near the optimal depth, where optical aberrations contribute negligibly and no additional correction is used. This is achieved by using a focusing lens with low NA. In the Supplementary Materials, we show the linear diffraction patterns for the arrays written at different depths. They clearly illustrate nearly identical shapes of the waveguide modes in different arrays and nearly identical diffraction rates. After the waveguide arrays were inscribed, the input/output facets of the sample were optically polished, so that the sample length was shortened to 99 mm.

Numerical simulations and normalizations

For numerical simulations of evolution and excitation of the nonlinear disclination states, we used dimensionless continuous nonlinear Schrödinger-like Eq. (1), in which the transverse coordinates x , y are normalized to the characteristic scale $r_0 = 10$ μm , the propagation distance z is normalized to the diffraction length $kr_0^2 \approx 1.14$ mm, $k = 2\pi n/\lambda$ is the wavenumber in the medium with the background refractive index n (for fused silica $n \approx 1.45$), and $\lambda = 800$ nm is the working wavelength. The dimensionless intensity $|\psi|^2$ corresponds to the intensity $I =$

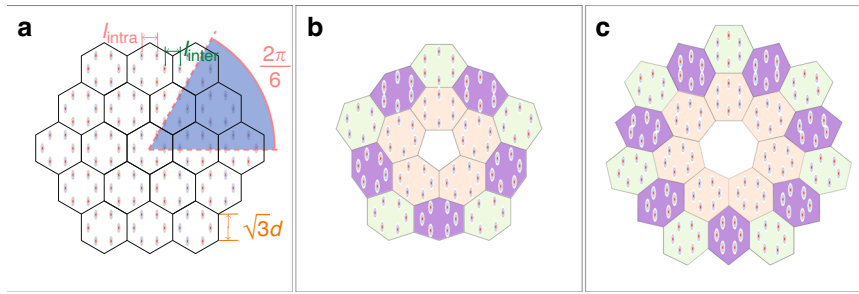


Fig. 6 Construction of the disclination array from honeycomb structure. **a** Original honeycomb array with intra-cell separation ℓ_{intra} and inter-cell separation ℓ_{inter} . The Kekulé distortion coefficient $r = \ell_{\text{intra}}/\ell_{\text{inter}}$. Each unit cell is indicated by white hexagons. $\sqrt{3}d$ denotes the length of one side of the hexagonal unit cell. **b** Disclination array with the pentagonal core obtained by removing the sector with the Frank angle $2\pi/6$ from array in **(a)** and gluing the cutting edges. **c** Disclination array with the heptagonal core obtained by inserting the sector with the Frank angle $2\pi/6$ into array **(a)** and subsequent compression of the unit cells. All arrays are shown within the window $-30 \leq x, y \leq 30$

$n|\psi|^2/k^2r_0^2n_2$, where n_2 is the nonlinear refractive index of the material (in fused silica $n_2 \approx 2.7 \times 10^{-20} \text{ m}^2/\text{W}$). Relation between the total beam power and the dimensionless power U is given by

$$\iint IdXdY = \frac{n}{k^2n_2} \iint |\psi|^2 dxdy = \frac{n}{k^2n_2} U$$

(here X, Y are the dimensional transverse coordinates). Since we work with the normalized quantities the results are applicable to materials with various nonlinear coefficients. Our waveguides are single-mode and elliptical due to the writing process, the dimensionless widths of the waveguides are $a_x = 0.25$ and $a_y = 0.75$ (corresponding to 2.5 and 7.5 μm , respectively), but the eigenmode of such waveguides is only slightly elliptical. The waveguide spacing in structure without distortion is $d = 3.2$ (corresponding to 32 μm). The array depth $p = k^2r_0^2\delta n/n$ is proportional to the refractive index contrast δn in the structure. For instance, $p = 1.0$ corresponds to $\delta n \sim 1.1 \times 10^{-4}$. In the majority of presented results (unless specifically stated in the caption), we use the depth $p = 5.0$ that provides the best agreement between experiments and theory.

Pentagonal and heptagonal disclination arrays were obtained from regular honeycomb arrays using two-step process described in the main text, when at the first stage by shifting the waveguides one introduces controllable Kekulé distortion, quantified by the distortion coefficient $r = \ell_{\text{intra}}/\ell_{\text{inter}}$, where ℓ_{intra} and ℓ_{inter} is the intra-cell and inter-cell spacing between waveguides after shift [see notations in Fig. 6a], while at the second stage one removes or inserts Frank sector into the array, and then expands or contracts unit cells such as to obtain the resulting disclination structure [Fig. 6b and c]. While deforming the structure we keep the longer axes of all elliptical waveguides parallel to the y axis.

Seeking for the spectrum presented in Fig. 1, we solve the linear version of Eq. (2) by using the plane-wave expansion method in which one expands u and \mathcal{R} into the Fourier series with the sufficient number of harmonics:

$$\begin{aligned} u &= \sum_{m,n} c_{m,n} e^{iK_m x + iK_n y} \\ \mathcal{R} &= \sum_{l,s} v_{l,s} e^{iK_l x + iK_s y} \end{aligned} \quad (3)$$

where $c_{m,n}$ and $v_{l,s}$ are the Fourier coefficients, $K_{m,l} = 2(m, l)\pi/D_x$, $K_{n,s} = 2(n, s)\pi/D_y$, $D_{x,y}$ are the sizes of the calculation window along the x, y axes, and (m, n, l, s) are integers. Plugging Eq. (3) into the linear version of Eq. (2), after simple algebraic transformations one obtains a series of linear equations with different (m, n, l, s) :

$$-\frac{1}{2}(K_m^2 + K_n^2)c_{m,n} + \sum_{l,s} v_{l,s} c_{m-l, n-s} = b c_{m,n} \quad (4)$$

Rewriting Eq. (4) in matrix format and diagonalizing the matrix, one obtains the eigenvalues b (i.e. the spectrum) and the corresponding eigenvectors $c_{m,n}$ that allow to construct the eigenmodes u of the array according to Eq. (3).

To obtain the families of the nonlinear states, we adopt the Newton relaxation method. In this method we transform Eq. (2) with included nonlinear term into a series of nonlinear equations $f_{m,n} = 0$ using the finite-difference approximation of derivatives:

$$\begin{aligned} f_{m,n}(\mathbf{u}) &= \frac{1}{2} \left(\frac{u_{m+1,n} - 2u_{m,n} + u_{m-1,n}}{dx^2} + \frac{u_{m,n+1} - 2u_{m,n} + u_{m,n-1}}{dy^2} \right) \\ &\quad + \mathcal{R}_{m,n} u_{m,n} + u_{m,n}^3 - b u_{m,n} \end{aligned} \quad (5)$$

where \mathbf{u} is a vector containing the values of the function $u_{m,n}$ on numerical grid, and (dx, dy) are the transverse steps. For each nonlinear equation, one finds the

corresponding element of the Jacobi matrix \mathbf{J} through

$$J_{(m,n),(p,q)} = \frac{\partial f_{m,n}(\mathbf{u})}{\partial u_{p,q}} \quad (6)$$

The method consists in generating solution of corresponding system of nonlinear equations using the iterative procedure

$$\mathbf{u}_{\text{new}} = \mathbf{u}_{\text{old}} - \mathbf{J}^{-1} \mathbf{f} \quad (7)$$

where \mathbf{f} is the vector with the elements given by Eq. (5). The iterations are stopped when the difference between solutions \mathbf{u}_{new} and \mathbf{u}_{old} reduces below the required level, typically below 10^{-10} .

Topological indices

The topological properties of disclination arrays can be discussed by analyzing the fractional “charge” that is carried by each unit cell, that is employed in established bulk-disclination correspondence principle²¹. Note that the “charge” here is spectral charge that can be defined through the local density of states. It is an analog of the real charge in electric systems, and it can be used to evaluate the number of states in the unit cell with states considered below the topological band gap²⁹. The spectral charge \mathcal{Q} bound to a disclination with a Frank angle Ω is defined by^{16,21–23,27,28}

$$\mathcal{Q} = \frac{\Omega}{2\pi} \left(\frac{3}{2} \chi_M - \chi_K \right) \text{ modulo } 1 \quad (8)$$

where the high symmetry indicators are $\chi_M = \#M_1^{(2)} - \#\Gamma_1^{(2)}$ and $\chi_K = \#K_1^{(3)} - \#\Gamma_1^{(3)}$ that should be calculated directly in the honeycomb array before removing or inserting the Frank sector. Here $\#\Pi_q^{(n)}$ is the number of bands below the forbidden gap at a high-symmetry point $\Pi = \Gamma, M, K$ with the eigenvalue of the C_n rotation matrix $e^{i2\pi(q-1)/n}$ ($q = 1, \dots, n$)²⁷, and $\Omega = 2\pi/6$ for the disclination arrays adopted in this work. For the topological nontrivial case with $r > 1$, one can find that $(\chi_M, \chi_K) = (2, 0)$ for both the pentagonal disclination array and the heptagonal disclination array. While for the topological trivial case with $r < 1$, $(\chi_M, \chi_K) = (0, 0)$. Thus, the fractional charge is $\mathcal{Q} = 1/2$ for $r > 1$ and $\mathcal{Q} = 0$ for $r < 1$. The fractional charge can be also obtained by counting the number of the Wannier centers occupied by each unit cell. The Wannier centers are located at the edges of the unit cell if $r > 1$ and at its center if $r < 1$. The unit cell around the pentagonal disclination core has five bulk Wannier centers if $r > 1$, which give a 5/2 charge per unit cell. If $r < 1$, the charge per unit cell around the disclination core is 3. See also the Supplementary Materials.

Acknowledgements

B.R., H.W. and Y.Z. acknowledge funding by the National Natural Science Foundation of China (Grant No.: 12074308) and the Fundamental Research

Funds for the Central Universities (Grant No.: xzy022022058). A.A.A., Y.V.K., S.A.Z., N.N.S., A.A.K., V.O.K., S.V.C., and V.N.Z. acknowledge funding by the Russian Science Foundation grant 21-12-00096 and by the research project FFUU-2021-0003 of the Institute of Spectroscopy of the Russian Academy of Sciences. A.A.K. and S.P.K. are supported by the Ministry of Science and Higher Education of the Russian Federation on the basis of the FSAEHE SUSU (NRU) (Agreement No.: 075-15-2022-1116).

Author details

¹Key Laboratory for Physical Electronics and Devices, Ministry of Education, School of Electronic Science and Engineering, Xi'an Jiaotong University, Xi'an 710049, China. ²Institute of Spectroscopy, Russian Academy of Sciences, Troitsk, Moscow 108840, Russia. ³Faculty of Physics, Higher School of Economics, Moscow 105066, Russia. ⁴Quantum Technology Centre, Faculty of Physics, M. V. Lomonosov Moscow State University, Moscow 119991, Russia

Author contributions

All authors made significant contribution to this work.

Conflict of interest

The authors declare no competing interests.

Supplementary information The online version contains supplementary material available at <https://doi.org/10.1038/s41377-023-01235-x>.

Received: 24 April 2023 Revised: 10 July 2023 Accepted: 14 July 2023

Published online: 10 August 2023

References

- Hasan, M. Z. & Kane, C. L. Colloquium: topological insulators. *Rev. Modern Phys.* **82**, 3045–3067 (2010).
- Qi, X.-L. & Zhang, S.-C. Topological insulators and superconductors. *Rev. Modern Phys.* **83**, 1057–1110 (2011).
- Huber, S. D. Topological mechanics. *Nat. Phys.* **12**, 621–623 (2016).
- Xue, H., Yang, Y. & Zhang, B. Topological acoustics. *Nat. Rev. Mater.* **7**, 974–990 (2022).
- Jotzu, G. et al. Experimental realisation of the topological Haldane model. *Nature* **515**, 237–240 (2014).
- Klembt, S. et al. Exciton-polariton topological insulator. *Nature* **562**, 552–556 (2018).
- Lu, L., Joannopoulos, J. D. & Soljačić, M. Topological photonics. *Nat. Photon.* **8**, 821–829 (2014).
- Ozawa, T. et al. Topological photonics. *Rev. Modern Phys.* **91**, 015006 (2019).
- Smirnova, D., Leykam, D., Chong, Y. & Kivshar, Y. Nonlinear topological photonics. *Appl. Phys. Rev.* **7**, 021306 (2020).
- Rechtsman, M. C. et al. Photonic Floquet topological insulators. *Nature* **496**, 196–200 (2013).
- Liang, G. Q. & Chong, Y. D. Optical resonator analog of a two-dimensional topological insulator. *Phys. Rev. Lett.* **110**, 203904 (2013).
- Wu, L.-H. & Hu, X. Scheme for achieving a topological photonic crystal by using dielectric material. *Phys. Rev. Lett.* **114**, 223901 (2015).
- Yang, Y. et al. Realization of a three-dimensional photonic topological insulator. *Nature* **565**, 622–626 (2019).
- Maczewsky, L. J., Zeuner, J. M., Nolte, S. & Szameit, A. Observation of photonic anomalous Floquet topological insulators. *Nat. Commun.* **8**, 13756 (2017).
- Noh, J., Huang, S., Chen, K. P. & Rechtsman, M. C. Observation of photonic topological valley Hall edge states. *Phys. Rev. Lett.* **120**, 063902 (2018).
- Noh, J. et al. Topological protection of photonic mid-gap defect modes. *Nat. Photon.* **12**, 408–415 (2018).
- Pyrilakos, G. G. et al. Bimorphic Floquet topological insulators. *Nat. Mater.* **21**, 634–639 (2022).
- Bandres, M. A., Rechtsman, M. C. & Segev, M. Topological photonic quasi-crystals: fractal topological spectrum and protected transport. *Phys. Rev. X* **6**, 011016 (2016).
- Yang, Z., Lustig, E., Lumer, Y. & Segev, M. Photonic Floquet topological insulators in a fractal lattice. *Light Sci. Appl.* **9**, 128 (2020).

20. Biesenthal, T. et al. Fractal photonic topological insulators. *Science* **376**, eabm2842 (2022).
21. Liu, Y. et al. Bulk-disclination correspondence in topological crystalline insulators. *Nature* **589**, 381–385 (2021).
22. Peterson, C. W., Li, T., Jiang, W., Hughes, T. L. & Bahl, G. Trapped fractional charges at bulk defects in topological insulators. *Nature* **589**, 376–380 (2021).
23. Wu, S., Jiang, B., Liu, Y. & Jiang, J.-H. All-dielectric photonic crystal with unconventional higher-order topology. *Photon. Res.* **9**, 668–677 (2021).
24. Rüegg, A. & Lin, C. Bound states of conical singularities in graphene-based topological insulators. *Phys. Rev. Lett.* **110**, 046401 (2013).
25. Teo, J. C. Y. & Hughes, T. L. Existence of Majorana-Fermion bound states on disclinations and the classification of topological crystalline superconductors in two dimensions. *Phys. Rev. Lett.* **111**, 047006 (2013).
26. Benalcazar, W. A., Teo, J. C. Y. & Hughes, T. L. Classification of two-dimensional topological crystalline superconductors and Majorana bound states at disclinations. *Phys. Rev. B* **89**, 224503 (2014).
27. Benalcazar, W. A., Li, T., Benalcazar, W. A., Hughes, T. L. Quantization of fractional corner charge in C_{3v} -symmetric higher-order topological crystalline insulators. *Phys. Rev. B* **99**, 245151 (2019).
28. Li, T., Zhu, P., Benalcazar, W. A. & Hughes, T. L. Fractional disclination charge in two-dimensional C_{3v} -symmetric topological crystalline insulators. *Phys. Rev. B* **101**, 115115 (2020).
29. Wang, H.-X. et al. Higher-order topological phases in tunable C_3 symmetric photonic crystals. *Photon. Res.* **9**, 1854–1864 (2021).
30. Peterson, C. W., Li, T., Benalcazar, W. A., Hughes, T. L. & Bahl, G. A fractional corner anomaly reveals higher-order topology. *Science* **368**, 1114–1118 (2020).
31. Xie, B. et al. Higher-order band topology. *Nat. Rev. Phys.* **3**, 520–532 (2021).
32. Chen, Y. et al. Observation of topological p -orbital disclination states in non-Euclidean acoustic metamaterials. *Phys. Rev. Lett.* **129**, 154301 (2022).
33. Wang, Q., Xue, H., Zhang, B. & Chong, Y. D. Observation of protected photonic edge states induced by real-space topological lattice defects. *Phys. Rev. Lett.* **124**, 243602 (2020).
34. Xie, B.-Y., You, O. & Zhang, S. Photonic topological pump between chiral disclination states. *Phys. Rev. A* **106**, L021502 (2022).
35. Wang, Q. et al. Vortex states in an acoustic Weyl crystal with a topological lattice defect. *Nat. Commun.* **12**, 3654 (2021).
36. Deng, Y. et al. Observation of degenerate zero-energy topological states at disclinations in an acoustic lattice. *Phys. Rev. Lett.* **128**, 174301 (2022).
37. Liang, S.-N. et al. Topological disclination states for surface acoustic waves. *Phys. Rev. B* **106**, 174112 (2022).
38. Ren, B., Wang, H., Kartashov, Y. V., Li, Y. & Zhang, Y. Nonlinear photonic disclination states. *APL Photon.* **8**, 016101 (2023).
39. Maczewsky, L. J. et al. Nonlinearity-induced photonic topological insulator. *Science* **370**, 701–704 (2020).
40. Jürgensen, M., Mukherjee, S. & Rechtsman, M. C. Quantized nonlinear Thouless pumping. *Nature* **596**, 63–67 (2021).
41. Fu, Q., Wang, P., Kartashov, Y. V., Konotop, V. V. & Ye, F. Nonlinear Thouless pumping: Solitons and transport breakdown. *Phys. Rev. Lett.* **128**, 154101 (2022).
42. Fu, Q., Wang, P., Kartashov, Y. V., Konotop, V. V. & Ye, F. Two-dimensional nonlinear Thouless pumping of matter waves. *Phys. Rev. Lett.* **129**, 183901 (2022).
43. Jürgensen, M., Mukherjee, S., Jörg, C. & Rechtsman, M. C. Quantized fractional Thouless pumping of solitons. *Nat. Phys.* **19**, 420–426 (2023).
44. Ablowitz, M. J., Curtis, C. W. & Ma, Y.-P. Linear and nonlinear traveling edge waves in optical honeycomb lattices. *Phys. Rev. A* **90**, 023813 (2014).
45. Leykam, D. & Chong, Y. D. Edge solitons in nonlinear-photonic topological insulators. *Phys. Rev. Lett.* **117**, 143901 (2016).
46. Ablowitz, M. J. & Cole, J. T. Tight-binding methods for general longitudinally driven photonic lattices: edge states and solitons. *Phys. Rev. A* **96**, 043868 (2017).
47. Lumer, Y., Plotnik, Y., Rechtsman, M. C. & Segev, M. Self-localized states in photonic topological insulators. *Phys. Rev. Lett.* **111**, 243905 (2013).
48. Zhang, Z. Y. et al. Observation of edge solitons in photonic graphene. *Nat. Commun.* **11**, 1902 (2020).
49. Mukherjee, S. & Rechtsman, M. C. Observation of Floquet solitons in a topological bandgap. *Science* **368**, 856–859 (2020).
50. Ivanov, S. K., Kartashov, Y. V., Szameit, A., Torner, L. & Konotop, V. V. Vector topological edge solitons in Floquet insulators. *ACS Photon.* **7**, 735–745 (2020).
51. Ivanov, S. K. et al. Topological dipole Floquet solitons. *Phys. Rev. A* **103**, 053507 (2021).
52. Zhong, H. et al. Nonlinear topological valley Hall edge states arising from type-II Dirac cones. *Adv. Photon.* **3**, 056001 (2021).
53. Ren, B. et al. Dark topological valley Hall edge solitons. *Nanophotonics* **10**, 3559–3566 (2021).
54. Kartashov, Y. V. & Skryabin, D. V. Modulational instability and solitary waves in polariton topological insulators. *Optica* **3**, 1228–1236 (2016).
55. Zhang, Y. Q., Kartashov, Y. V. & Ferrando, A. Interface states in polariton topological insulators. *Phys. Rev. A* **99**, 053836 (2019).
56. Kartashov, Y. V. & Skryabin, D. V. Bistable topological insulator with exciton-polaritons. *Phys. Rev. Lett.* **119**, 253904 (2017).
57. Zhang, W., Chen, X., Kartashov, Y. V., Skryabin, D. V. & Ye, F. Finite-dimensional bistable topological insulators: from small to large. *Laser Photon. Rev.* **13**, 1900198 (2019).
58. Zhang, Y., Kartashov, Y. V., Torner, L., Li, Y. & Ferrando, A. Nonlinear higher-order polariton topological insulator. *Optics Lett.* **45**, 4710–4713 (2020).
59. Kirsch, M. S. et al. Nonlinear second-order photonic topological insulators. *Nat. Phys.* **17**, 995–1000 (2021).
60. Hu, Z. et al. Nonlinear control of photonic higher-order topological bound states in the continuum. *Light Sci. Appl.* **10**, 164 (2021).
61. Zhong, H., Kartashov, Y. V., Li, Y. & Zhang, Y. π -mode solitons in photonic Floquet lattices. *Phys. Rev. A* **107**, L021502 (2023).
62. Kartashov, Y. V. et al. Observation of edge solitons in topological trimer arrays. *Phys. Rev. Lett.* **128**, 093901 (2022).
63. Tan, D., Wang, Z., Xu, B. & Qiu, J. Photonic circuits written by femtosecond laser in glass: improved fabrication and recent progress in photonic devices. *Adv. Photon.* **3**, 024002 (2021).
64. Lin, Z. & Hong, M. Femtosecond laser precision engineering: from micron, submicron, to nanoscale. *Ultrafast Sci.* **2021**, 9783514 (2021).
65. Li, L., Kong, W. & Chen, F. Femtosecond laser-inscribed optical waveguides in dielectric crystals: a concise review and recent advances. *Adv. Photon.* **4**, 024002 (2022).
66. Lederer, F. et al. Discrete solitons in optics. *Phys. Rep.* **463**, 1–126 (2008).
67. Fu, Q. et al. Optical soliton formation controlled by angle twisting in photonic moiré lattices. *Nat. Photon.* **14**, 663–668 (2020).
68. Qin, H., Zhang, Z., Chen, Q. & Fleury, R. Anomalous Floquet topological disclination states. Print at <https://doi.org/10.48550/arXiv.2304.03206> (2023).